Materials Today Bio 32 (2025) 101778

Contents lists available at ScienceDirect

Materials Today Bio

journal homepage: www.journals.elsevier.com/materials-today-bio

Membrane biomimetic nanoenzyme-incorporated hybrid glycyrrhizic acid hydrogel for precise mitochondrial ROS scavenging for osteoarthritis treatment

Yong Fan [a,b,c,d,1], Zexuan Niu [a,b,c,d,1], Li Yin [a,b,c,d,1], Longtao Yao [a,b,c,d], Sheyuan Ding [a,c,d], Yu Tong [a,c,d], Jiao Wang [a,c,d], Zheping Hong [a,c,d], Jihang Chen [a,c,d], Qiong Zhang [e], Lichen Ji [f], Jiaxin Chen [g,*], Chen Xia [a,c,d,**], Qing Bi [a,b,c,d,***]

[a] Department of Sports Medicine, Zhejiang Provincial People's Hospital (Affiliated People's Hospital), Hangzhou Medical College, Hangzhou, Zhejiang, 310000, China
[b] Postgraduate training base Alliance of Wenzhou Medical University, Wenzhou, Zhejiang Province, 325000, China
[c] Center for Rehabilitation Medicine, Department of Orthopedics, Zhejiang Provincial People's Hospital, Hangzhou Medical College, Hangzhou, Zhejiang, 310000, China
[d] Institute of Sports Medicine and Osteoarthropathy of Hangzhou Medical College, Hangzhou, Zhejiang, 310000, China
[e] Department of Nursing, Zhejiang Provincial People's Hospital (Affiliated People's Hospital), Hangzhou Medical College, Hangzhou, Zhejiang, 310000, China
[f] Department of Joint Surgery, Shanghai East Hospital, Tongji University School of Medicine, Shanghai, 200092, China
[g] Center for Plastic & Reconstructive Surgery, Department of Plastic & Reconstructive Surgery, Zhejiang Provincial People's Hospital (Affiliated People's Hospital), Hangzhou Medical College, Hangzhou, 310000, China

ARTICLE INFO

Keywords:
Osteoarthritis
Mitochondrial ROS
Cytomembrane
Mitochondrial targeting
STING

ABSTRACT

Osteoarthritis (OA) is a progressive degenerative disorder which severely threatens the quality of life of older individuals. OA progression is closely related to heightened levels of mitochondrial reactive oxygen species (mtROS). Although nanozymes have a good ROS-scavenging effect, they cannot precisely scavenge mtROS because of the immune rejection of cell membranes, lysosomal escape, and the inability of conventional nanozymes to directly target mitochondria. Dual-target nanozymes were engineered to precisely scavenge mtROS in chondrocytes. We used chondrocyte membrane-camouflaged TPP-modified hollow Prussian blue nanozymes and subsequently encapsulated these nanozymes in a hybrid glycyrrhizic acid hydrogel. The therapeutic efficacy and underlying mechanisms were assessed in vitro and in vivo. The novel nanozymes enhanced cell selectivity, immune evasion capabilities, and mitochondrial targeting. The dual-targeted nanozymes exerted a pronounced therapeutic impact on inflammatory chondrocytes, mitigated mtDNA leakage by precisely scavenging mtROS, dampened cGAS-STING-NF-κB signaling, and enhanced chondrocyte function. The hybrid hydrogels also exhibited improved therapeutic outcomes. We confirmed the beneficial effects of the nanozyme-hydrogel combination on OA progression in mice. The nanozyme-hydrogel combination can reduce precisely scavenge mtROS in chondrocytes, avoiding the leakage of mtDNA and suppressing the cGAS-STING-NF-κB signaling pathway, thereby decreasing inflammatory responses and alleviate OA progression.

Abbreviations: OA, Osteoarthritis; Bovine serum albumin, (BSA); Chondrocyte membrane-disguised HPBPT, (CM@HPBPT); Dulbecco's modified Eagle's medium, (DMEM); Fetal bovine serum, (FBS); fluorescein isothiocyanate, (FITC); GA-GelMA, (GGM); Gelatin methacryloyl, (GelMA); Glycyrrhizic acid, (GA); Hematoxylin and eosin, (HE); Hollow Prussian blue, (HPB); laser confocal microscope, (LCM); mitochondrial permeability transition pore, (mPTP); Mitochondrial ROS, (mtROS); Osteoarthritis, (OA); PEI-TPP-modified HPB, (HPBPT); reactive oxygen species, (ROS); Transmission electron microscope, (TEM); IL-1β, Interleukin-1β; mtDNA, Mitochondrial DNA; BV/TV, Bone volume fraction; Tb.Pf, trabecular pattern factor; SO, Safranin O - Fast green staining; SEM, Scanning Electron Microscope.

* Corresponding author. Center for Plastic & Reconstructive Surgery, Department of Plastic & Reconstructive Surgery, Zhejiang Provincial People's Hospital (Affiliated People's Hospital), Hangzhou Medical College, Hangzhou, 310000, China.
** Corresponding author. Department of Sports Medicine, Zhejiang Provincial People's Hospital (Affiliated People's Hospital), Hangzhou Medical College, Hangzhou, Zhejiang, 310000, China.
*** Corresponding author. Department of Sports Medicine, Zhejiang Provincial People's Hospital (Affiliated People's Hospital), Hangzhou Medical College, Hangzhou, Zhejiang, 310000, China.
E-mail addresses: cjx21918392@163.com (J. Chen), 497077831@qq.com (C. Xia), bqzjsrmyy@163.com (Q. Bi).
[1] These authors contributed equally to this study.

https://doi.org/10.1016/j.mtbio.2025.101778
Received 30 December 2024; Received in revised form 13 April 2025; Accepted 17 April 2025
Available online 17 April 2025

1. Introduction

Osteoarthritis (OA) is a degenerative joint disorder predominantly associated with aging, obesity, and metabolic factors [1]. As the global population exposed to these risk factors increases, the annual OA incidence has become prevalent, thereby exacerbating both personal and societal burdens [2]. OA is characterized by joint inflammation and progressive cartilage deterioration, with cartilage degeneration being a pivotal factor in disease progression [3]. Enzymes responsible for cartilage extracellular matrix (ECM) degradation, such as ADAMTS-5, and MMP-13, are upregulated in inflammatory degenerative chondrocytes [4]. Conversely, components in the synthesis of ECM, including aggrecan and collagen II, are downregulated [5]. Despite these insights, the precise etiology of OA remains unclear. Existing clinical treatments, including hyaluronic acid and anti-inflammatory medications, have limited efficacy in curbing the progression of OA [6]. Consequently, potent therapeutics are urgently needed to mitigate OA progression.

Mitochondria are double-membrane organelles with the capacity for the autonomous replication of mitochondrial DNA (mtDNA) [7] and serve as the principal producers of reactive oxygen species (ROS) [8]. Previous research has indicated a significant link between ROS levels and the pathological processes of OA [9]. An imbalance between mitochondrial ROS (mtROS) production and removal results in uncontrolled inflammation and OA progression [10]. Emerging evidence suggests that in a spectrum of inflammatory degenerative diseases, the accumulation of excessive mtROS triggers the opening of the mitochondrial permeability transition pore (mPTP) [11], resulting in the transportation of mtDNA into the cytoplasm [12]. The cGAS-STING signaling pathway activated by cytosolic mtDNA [13] results in the NF-κB signaling cascade activation and the onset of an inflammatory response [14,15]. Therefore, a promising therapeutic strategy for ameliorating OA progression involves the targeted elimination of mtROS in chondrocytes to curtail the inflammatory response induced by mtDNA release.

In recent years, with the continuous advancement of therapeutic strategies, the development of conventional materials such as extracellular vesicles, hydrogels, and nanoparticles has brought new breakthroughs in OA treatment [16–18]. These materials delay OA progression through various approaches including sustained release, targeted delivery, and modulation of the cartilage microenvironment, while also providing precise therapeutic tools for subsequent pathological interventions in OA [19]. Multiple metallic nanozymes such as MnO2 and CeO2 typically exhibit excellent ROS scavenging capabilities and are widely applied in OA treatment. [20]. Among these, Hollow Prussian blue (HPB) nanozymes have been distinguished as efficacious nanozymes owing to their hollow mesoporous architecture and exceptional ROS-scavenging capabilities [21]. Previous studies have demonstrated the ability of PB nanozymes to delay OA progression by scavenging ROS [22]. However, despite the good ROS-scavenging ability of metal nanozymes, their applications are often limited by problems such as immune rejection and lysosomal degradation. Most metal nanozymes are internalized through endocytosis and degraded via lysosomal phagocytosis, limiting their ability to reach the cytoplasm and hampering their therapeutic efficacy [23]. Therefore, the targeted removal of mtROS from specific cells remains a major challenge. Recent studies have suggested that coating cell membranes with nanozymes can facilitate efficient cellular delivery and prevent lysosomal degradation [24]. This approach offers a promising strategy for HPB to enter the cytoplasm and exert its effects. However, because mitochondria are negatively charged double-membrane organelles, it is difficult for negatively charged metal nanozymes to approach the mitochondria [25]. Additionally, the lipotropic cationic properties of (3-carboxypropyl)- triphenylphosphonium bromide (TPP) can facilitate mitochondrial targeting [26,27].

Previous applications of metal nanozymes have been limited by their short action times and high toxicity [28]. Hydrogels have demonstrated unique advantages in cartilage tissue engineering owing to their drug sustained-release capability, excellent biocompatibility, and ECM-like properties, offer a potential strategy to solve existing challenges [29–31]. Glycyrrhizic Acid (GA), a natural compound derived from the traditional Chinese herb Glycyrrhiza, features a molecular structure rich in hydroxyl and carboxyl groups. It not only demonstrates potent anti-inflammatory activity but also reduces the friction coefficient of hydrogels [32]. However, its low mechanical strength has hindered its practical application. Gelatin Methacryloyl (GelMA) has garnered significant attention for its superior photo-crosslinking properties and tunable physicochemical characteristics [33]. Through photoinitiated crosslinking, GelMA forms a stable network structure that markedly enhances the mechanical strength of hydrogels [34,35]. Therefore, we developed a GA-GelMA hydrogel that integrates both mechanical strength and anti-inflammatory properties.

In this study, we used PEI in combination with TPP to enhance its cationic properties and developed PEI-TPP-modified HPB (HPBPT) to realize mitochondrial targeting. Thus, we synthesized chondrocyte membrane-disguised HPBPT (CM@HPBPT) to enable the delivery of HPBPT to the cytoplasm and precisely target the mitochondria. Chondrocyte membranes were extracted using ultrasonic crushing. PEI was chemically conjugated with TPP to obtain PEI-TPP. The synthesized HPB nanozymes, with efficient ROS-scavenging ability, were modified with PEI-TPP (HPBPT) to enable mitochondrial targeting. HPBPT was then camouflaged with the extracted chondrocyte membranes to create CM@HPBPT, which targeted chondrocytes and facilitated the cytoplasmic delivery of HPBPT, bypassing lysosomal degradation. CM@HPBPT was incorporated with the GA multifunctional hydrogel enhanced with GelMA (GGM@CM@HPBPT), which was injected into the joint cavity of OA mice.

2. Materials and methods

2.1. Materials and reagents

Dulbecco's modified Eagle's medium (DMEM)/F12 and fetal bovine serum (FBS) were obtained from Gibco (CA, USA). Recombinant mouse IL-1β protein, chlorpromazine, filipin III, wortmannin, cytochalasin D, the ECL Kit, glycyrrhizic acid and the JC-1 Assay Kit were produced by MedChemExpress (Shanghai, China). Fluorescent dyes for labeling various cellular components, including DiO, DiI, Lyso-Tracker Red, Mito-Tracker Red, DAPI, Hoechst, and Mitosox Red were acquired from Beyotime (Shanghai, China). The CCK-8, Reverse Transcription Kit, type II collagenase, phenylmethylsulfonyl fluoride (PMSF), SYBR Green Mix were all purchased from Yeason (Shanghai, China). $K_3[Fe(CN)_6]\cdot 3H_2O$, poly(vinylpyrrolidone) (PVP, K30), PEI, TPP, and methacrylate gelatin were all purchased from Aladdin (Shanghai, China). Antibodies specific for β-actin, Na^+/K^+-ATPase, α-tubulin, matrix metalloproteinase-13 (MMP-13), aggrecan, TOM-20, phosphorylated IkB (p-IkBα), IkBα, stimulator of interferon genes (STING), and lamin b1 were acquired from Proteintech (Wuhan, China). Antibodies against collagen II, ADAMTS-5, P65, phosphorylated p65 (p-P65), and 8-hydroxydeoxyguanosine (8-OHdg) were produced by Abcam (UK). The cGAS antibody was sourced from ABclonal (China), the phosphorylated STING (p-STING) antibody was from Affinity (Jiangsu, China), and the anti-DNA antibody was obtained from Millipore (Massachusetts, USA). Primer sequences are provided in Supplementary Table 1.

2.2. Animal experiment

Eight-week-old mice (C57BL/6, male) were categorized into 10 groups (n = 5) under standard environmental conditions. This study was approved by the Zhejiang Provincial People's Hospital Committee for Animal Experimentation (ethics code: 20231129202647161557). All animal procedures adhered to the institutional guidelines. Anterior cruciate ligament transection (ACLT) surgery was performed to establish

the mice model of OA [36]. An identical surgical technique was used for the sham-operated mice without ACL transection. Upon undergoing surgery, the animals were grouped randomly into: Sham, ACLT (untreated), ACLT treated with the GGM hydrogel (GGM), ACLT treated with CM@HPBPT nanoparticles (CM@HPBPT), and ACLT treated with the GGM@CM@HPBPT composite hydrogel (GGM@CM@HPBPT). Three days post-surgery, treatment was initiated via intra-articular injections (20 μL, 80 μg/mL, soluble in saline) administered weekly. At the end of 4 and 8 weeks, all experimental animals were euthanized, and their joints were collected and preserved in 4 % PFA for 2 days.

2.3. Cell culture

The articular cartilage was extracted from the tibial plateau and femoral condyles of 5-day-old male C57BL/6 mice. The tissue was initially rinsed with PBS, followed by enzymatic digestion with 0.25 % collagenase type II at 37 °C for 3 h. Post-centrifugation (300 g, 5 min), the liberated chondrocytes were plated and propagated in DMEM/F12 supplemented with 10 % FBS at 37 °C. Chondrocytes from the second passage were employed in later experiments.

2.4. Synthesis of CM@HPBPT nanozymes

2.4.1. Preparation of chondrocyte membrane (CM)

Based on a previously published protocol [37], chondrocytes were homogenized in an isolation buffer (0.5 mM ethylenediaminetetraacetic acid (EDTA), 30 mM Tris-HCl, 225 mM mannitol, 0.5 % (w/v) bovine serum albumin (BSA), 75 mM sucrose, and 1 % PMSF). Cell disruption was achieved by ultrasonication (35 W) for 0.5 h. The homogenates were centrifuged at 800g for 0.25 h and the supernatant was obtained for another centrifugation at 10,000g for 0.5 h. The supernatant was subjected to ultracentrifugation at 100,000g for 1.5 h. Upon removing the supernatant, the CM nanoparticles (NPs) were gathered and reserved at −80 °C.

Preparation of HPB nanozymes: The HPB NPs were synthesized following a previously described method [38]. PVP (3 g) and $K_3[Fe(CN)_6]\cdot 3H_2O$ (131.72 mg) were supplement to 40 mL of a 0.01 M HCl solution and stirred for 0.5 h. The mixture was heated at 80 °C for 1 day. Following centrifugation, the product was washed and dried. Subsequently, dry PB NPs (20 mg) and PVP (100 mg) were incorporated into a 1 M HCl aqueous solution (20 mL) in a Teflon vial. The mixture was heated to 140 °C for 4 h. The HPB NPs were centrifugated for isolation and washed.

2.4.2. Preparation of HPBPT nanozymes

TPP (429.29 mg), EDC (191 mg), and NHS (115 mg) were placed in DMSO (20 mL), followed by stirring for 1 h. Subsequently, 10 kDa PEI (86 mg) was supplemented to the solution and stirred for 1.5 h. Subsequently, the mixture was dialyzed using cellulose ester membranes with a 3.5 kDa molecular weight cutoff and lyophilized. The products were characterized by ^{1}H NMR and FTIR (Thermo). Finally, PEI-TPP (PT, 20 mg) and HPB NPs (10 mg) were dissolved in water (10 mL) and sonicated for 0.5 h. The resulting HPB-PT nanozymes (10 mg) were collected via centrifugation.

2.4.3. Synthesis of CM@HPBPT nanozymes

The BCA Assay Kit was deployed to assess the content of chondrocyte membrane protein. Specifically, 0.5 mL of 1 mg/mL HPBPT was supplemented to the same amount of CM NPs solution with the same concentration. The mixture was sonicated (30 W) for 10 min and then extruded through a 400 nm cutoff membrane (Hamilton, USA) for 30 passes. The HPBPT-encapsulated CM (CM@HPBPT) was recovered via centrifugation at 10,000g for 10 min.

2.5. Characterization of the CM@HPBPT nanozymes

Transmission electron microscopy (TEM, Hitachi, Japan) was utilized to characterize the morphology of the CM@HPBPT nanozymes. The radii and zeta potentials of the NPs were measured using dynamic light scattering (DLS, China). The UV–visible spectra (PE Lambda 750, China) of the NPs were acquired to analyze their absorption properties.

2.6. Cell viability assay

The chondrocytes were placed in 96-well plates (7500 cells per well). Based on 24 h incubation at 37 °C, treatments were performed at the indicated concentrations (0, 40, 80,160, 320 μg/ml). CCK-8 assay was performed following another round of incubation for 24 h. The plates were then kept at 37 °C for incubation, and cell viability was assessed using a microplate reader (BioTek, USA).

2.7. Selectivity of cellular uptake of CM@HPBPT nanozymes

Chondrocytes and RAW 264.7 macrophages were used to evaluate the effects of membrane coatings on cellular uptake. They were placed into confocal dishes (8×10^4 cells per well) and cultured for 24 h. HPBs were first labeled with fluorescein isothiocyanate (FITC) before being coated with CM NPs. The NPs were then incubated with the chondrocytes and RAW 264.7 macrophages for 6 h. Following washing with PBS, the cells were stained with Hoechst for 10 min for nuclear visualization. The images were captured utilizing a laser confocal microscopy (LCM, Nikon, Japan).

2.8. Membrane fusion of CM@HPBPT nanozymes

Chondrocytes were introduced into confocal dishes (8×10^4 cells/well) for 24 h. Subsequently, the chondrocytes were labeled with DiI, and CM@HPBPT was labeled with DiO. Following incubation for 1 h, the cells were thoroughly washed with PBS three times. The labeled CM@HPBPT was then supplemented to the chondrocyte cultures and incubated for an additional hour. Following another round of washing with PBS, the cells were maintained by Hoechst stain for 10 min. Finally, the chondrocytes were visualized using the LCM.

2.9. Efficacy of endocytosis inhibitors on the cellular uptake of CM@HPBPT nanozymes

Chondrocytes were placed on 12-well plates (8×10^4 cells/well). The chondrocytes were then placed at 4 °C or separately cultured with one of the four endocytosis inhibitors for 1 h at 37 °C: cytochalasin D (5 μM) to inhibit phagocytosis, wortmannin (5 μM) to inhibit macropinocytosis, filipin III (7.5 μM) to inhibit caveolae-dependent endocytosis, or chlorpromazine (50 μM) to inhibit clathrin-dependent endocytosis. Following inhibitor treatment, the medium was supplemented with labeled CM@HPBPT for an additional 6 h at 37 °C. Images were captured using LCM.

2.10. In-vitro lysosome escape study

Lysosomal escape was evaluated based on a previous study [24]. Chondrocytes were plated in confocal dishes (8×10^4 cells/well) for a 24-h incubation. Subsequently, the culture medium was substituted with media containing either CM@HPBPT or HPBPT, and the cells were cultured for an additional 4 h. Lysosomes were then stained with LysoTracker Red for 30 min, followed by Hoechst staining of the cell nuclei for 10 min. Images were captured using the LCM.

2.11. In-vitro mitochondrial targeting study

Mitochondrial targeting was evaluated based on a previous study

[39]. Chondrocytes were plated in confocal dishes (8×10^4 cells/well) for 24-h incubation. The cells were then cultured with a medium containing either CM@HPBPT or CM@HPB for 6 h. The mitochondria were stained with MitoTracker Red for 25 min, followed by Hoechst staining of the cell nuclei for 10 min. Images were captured using the LCM.

2.12. RT-qPCR experiments

Total RNA was extracted from the chondrocytes utilizing the RNA extraction kit (ESScience, China), and RNA (1000 ng) was applied for the synthesis of cDNA. RT-qPCR was conducted using the Roche System (LightCycler 480 II) with 10 μL (5 μL SYBR Green Master Mix, 4.6 μL diluted cDNA, 0.2 μL reverse primer, and 0.2 μL forward primer). Expression of all target genes was normalized to the GAPDH expression. The sequences of primers for the target genes are provided in Supplementary Table 1.

2.13. Quantification of mtDNA release

As previously reported [40], the cytoplasmic components were isolated using digitonin lysis and centrifuged at 800g for 10 min. The supernatant was subjected to 0.5 h of centrifugation at 15,000g. The protein concentration was then identified based on the BCA assay kit (Thermo Fisher, US), and samples were normalized. DNA was extracted from equal amounts of the cytoplasmic components utilizing a commercially available DNA extraction kit (Qiagen, Hilden, Germany). The level of D-loop was then detected using quantitative PCR to evaluate the extent of mtDNA leakage.

2.14. Western blot

Chondrocytes underwent lysis with the application of radioimmunoprecipitation assay (RIPA) buffer (1 % PMSF). Proteins (30 μg) were processed through sodium dodecyl sulfate polyacrylamide gel electrophoresis and transferred onto polyvinylidene fluoride membranes. Following a 1.5-h blocking period with 5 % BSA and washing with tris-buffered saline with Tween-20 (TBST), the membranes were left with specific primary antibodies overnight at 4 °C, with TBST wash and another 1.5 h of incubation with the secondary antibodies. Finally, protein signals were examined using an ECL kit and images were captured using Image Lab (Bio-Rad).

2.15. Preparation and characterization of the hybrid hydrogel

A solution of gelatin methacrylate (GelMA, 6 % w/v) containing GA (1 % w/v) and zinc sulfate (500 μg/mL) was heated to 85 °C and thoroughly mixed to form a pre-hydrogel solution. The solution was then cooled to 37 °C, and CM@HPBPT was supplement to obtain the GGM@CM@HPBPT composite hydrogel. Upon cooling to room temperature, the GA self-assembled to form a primary network within the hydrogel. However, the network exhibited limited mechanical strength and became brittle upon freeze drying. Subsequent exposure to ultraviolet light (10 s) initiated crosslinking of the Gel-MA component, inducing the formation of a secondary network and a significant enhancement in the overall hydrogel strength. The gelation behavior and injectability of the prepared hydrogels were evaluated. The freeze-dried hydrogels were characterized based on the Fourier transform infrared (FTIR) spectroscopy (Thermo Nicolet) to analyze their chemical compositions. Additionally, the microstructures of the hydrogels were visualized using scanning electron microscopy (SEM; Hitachi, Japan). The rheological behavior of the hydrogels (1.5 mL) was evaluated using a rheometer (Haake Mars40, Germany). The shear frequency was varied logarithmically from 1 to 100 rad/s at a constant strain of 1 %.

2.16. Swelling tests

The lyophilized hydrogels (W_0) were soaked up under the 3 mL of PBS at 37 °C. The hydrogels were carefully removed at certain time points, and excess surface water was eliminated using absorbent paper. The weight (W_t) of the swollen hydrogels was recorded. The hydrogel swelling ratio (SR) was determined using the following formula: $SR = (W_t - W_0)/W_0 \times 100\ \%$.

2.17. Biocompatibility of the hybrid hydrogels in vitro

Chondrocytes were placed into 48-well plates (1×10^5 cells per well). Following 24 h of incubation with the hydrogels in Transwell inserts, the inserts were removed, and a live/dead assay kit (Beyotime) was performed to assess cell cytotoxicity.

2.18. Micro-CT image analysis

To assess OA progression, the tibial subchondral bone was examined using micro-computed tomography (micro-CT) as previously reported [41].The knee joints were imaged and analyzed using micro-CT (Skyscan 1275). The entire tibial subchondral bone medial compartment was considered as the region of interest, and the three-dimensional (3D) structural parameters analyzed included bone volume fraction and trabecular pattern factor.

2.19. Histological analysis

The joints were processed for decalcification in 10 % EDTA solution for 2 months and dehydrated using graded ethanol. The tissues were then fixed in paraffin and sliced into 5 μm sections. They were stained with hematoxylin and eosin (HE) and Safranin O-Fast Green staining (SO). The degree of osteoarthritis in the joints was evaluated using the OARSI (0–6) grading method [42].

2.20. Immunofluorescence (IF) staining assay

Following fixation with 4 % PFA for 0.5 h, the cells were permeabilized with 0.25 % Triton X-100 for 0.5 h. Subsequently, the cells were treated with 5 % BSA for 1-h blocking and incubated with specific primary antibodies. Following the washing process, they were stained with the appropriate secondary antibodies and DAPI. Images were captured using the LCM. For tissues, sections were dewaxed and repaired with 10 % EDTA, blocked with 5 % BSA for 0.5 h, incubated with specific primary antibodies overnight at 4 °C, and then stained with the appropriate secondary antibodies and DAPI. Images were captured using a scanning system (Panoramic MIDI).

2.21. Safety evaluation in vivo

Following euthanasia, the organs (kidneys, spleen, liver, lungs, and heart) were obtained and processed by HE staining to assess systemic toxicity.

2.22. Statistics

All data are presented as the mean ± standard deviation (SD). Statistical analyses were conducted utilizing GraphPad Prism 10.0. Student's *t*-test was applied to compare data between two independent groups. Analysis of variance (ANOVA) followed by Tukey's multiple comparison test was performed to compare data between multiple groups. $p < 0.05$ represented statistical significance. Significance levels are signified by *: ***$p < 0.001$, **$p < 0.01$, *$p < 0.05$, and ns, non-significant.

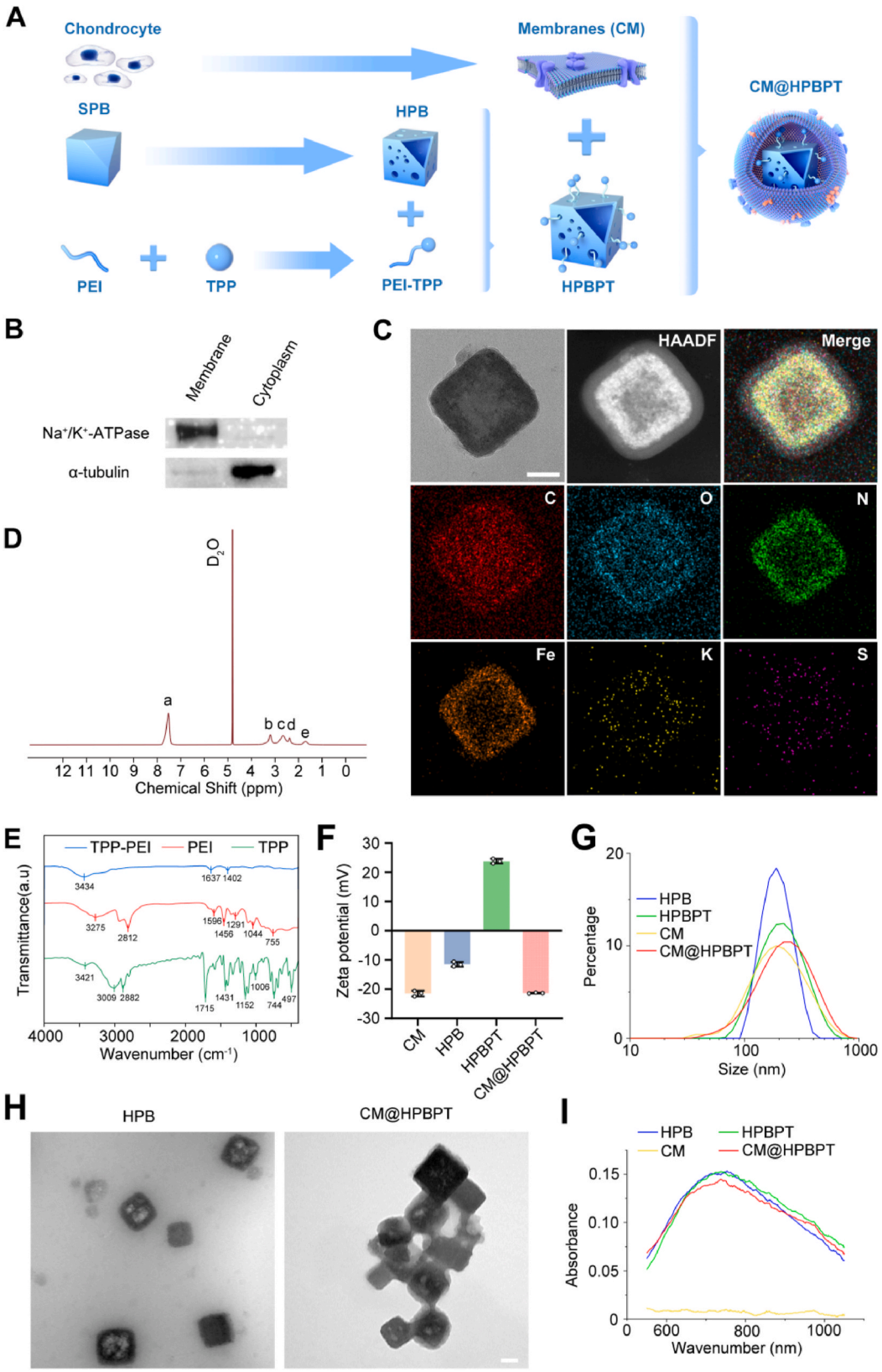

Fig. 1. Preparation and characterization of CM@HPBPT nanozymes. (A) Schematic illustration of CM@HPBPT synthesis. (B) Western blot images of α-tubulin and Na+/K + - ATPase. (C) High-resolution TEM images and element mapping (C, O, N, Fe, K, and S) of HPB nanozymes (scale bar, 50 nm). (D) ^{1}H NMR for PEI-TPP (a, 7.53 ppm; b, 3.20 ppm; c, 2.66 ppm; d, 2.37 ppm; e, 1.70 ppm). (E) FTIR spectra for PEI-TPP. (F) Zeta potentials of HPB, HPBPT, CM, and CM@HPBPT (n = 3). (G) Diameters of HPB, HPBPT, CM, and CM@HPBPT. (H) TEM images of HPB and CM@HPBPT (scale bar, 50 nm). (I) Ultraviolet absorption spectra of HPB, HPBPT, CM, and CM@HPBPT.

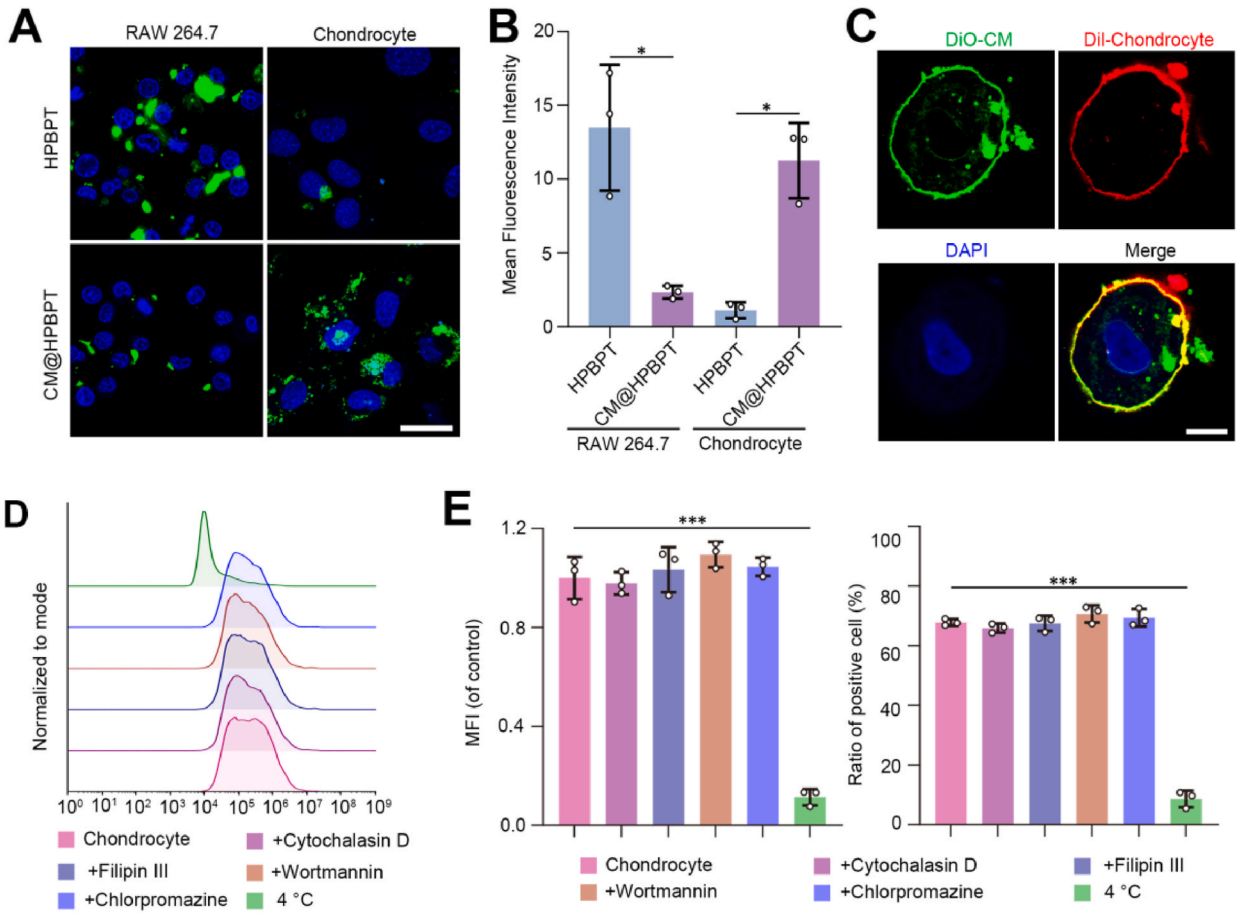

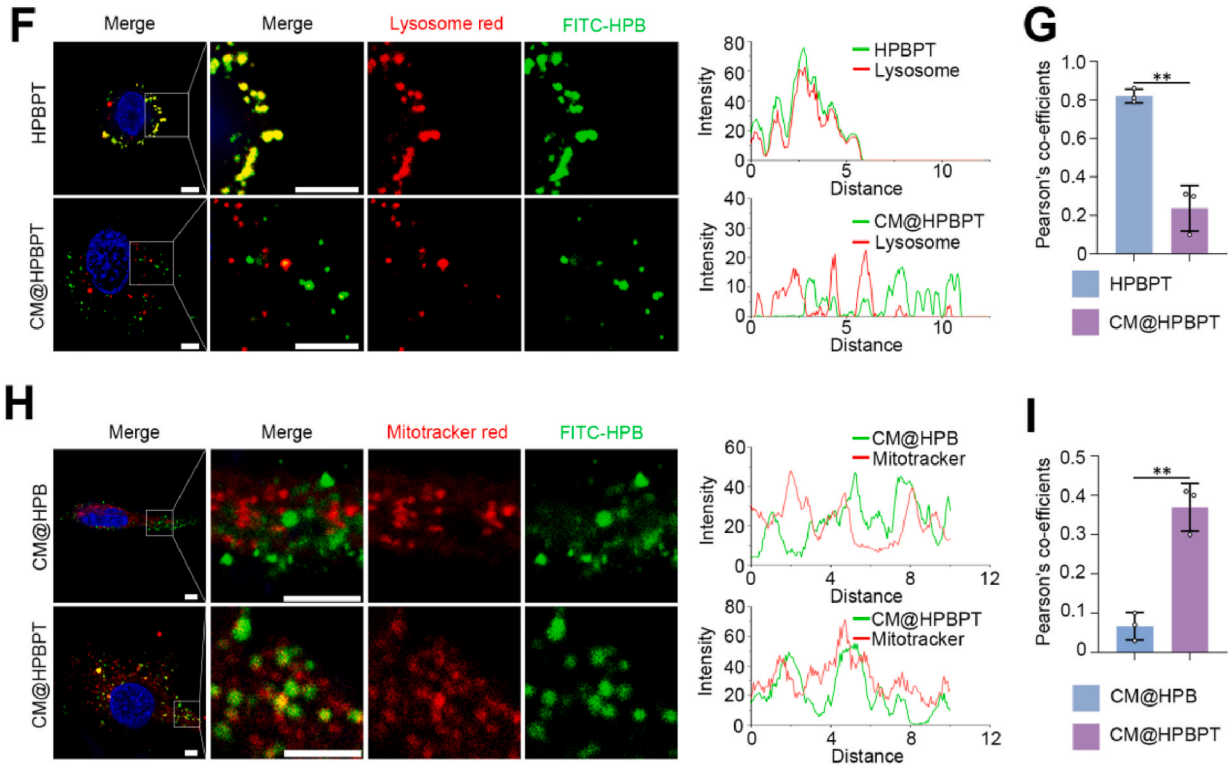

(caption on next page)

Fig. 2. Chondrocyte membrane fusion, intracellular release pathway, and mitochondrial targeting of CM@HPBPT nanozymes. (A) Uptake of HPBPT and CM@HPBPT by chondrocytes or RAW 264.7 macrophages. HPBPT, green; nuclei, blue (scale bar, 25 nm). (B) Mean fluorescence intensity (MFI) of HPBPT and CM@HPBPT uptake by chondrocytes or macrophages (n = 3). (C) Confocal microscopy images suggesting the correlation between the DiI-labeled chondrocyte membrane and DiO-labeled CM NPs (Chondrocyte membrane, red; CM NPs, green; nuclei, blue. Scale bar, 10 μm). (D) Positive cells detected using flow cytometry following CM@HPBPT therapy (labeled HPBPT). (E) MFI (left) and ratio of positive chondrocytes (right) (n = 3). (F) Confocal microscopy images (left) indicating the localization of HPBPT and lysosome after incubation with HPBPT or CM@HPBPT (lysosome, red; HPBPT, green; nuclei, blue. Scale bar, 5 μm) and intensity profiles (right). (G) Pearson's coefficients of the HPBPT and lysosomes (n = 3). (H) Confocal microscopy images (left) indicating the localization of HPB and mitochondria after incubation with CM@HPB or CM@HPBPT (mitochondria, red; HPB, green; nuclei, blue. Scale bar, 5 μm) and their intensity profiles (right). (I) Pearson's coefficients of the HPB and mitochondria (n = 3). ***p < 0.001; **p < 0.01; *p < 0.05. (For interpretation of the references to colour in this figure legend, the reader is referred to the Web version of this article.)

3. Results and discussion

3.1. Synthesis and characterization of CM@HPBPT nanozymes

We designed CM@HPBPT (Fig. 1A) to achieve precise scavenging of mtROS in chondrocytes. First, the chondrocytes were purified, and their membranes were isolated. The level of Na^+/K^+-ATPase in the CM NPs, assessed using western blotting, was higher than that in the cytoplasm, confirming successful separation (Fig. 1B). Subsequently, the HPB nanozymes were synthesized for efficient ROS scavenging. High-resolution TEM revealed a uniform cubic shape (approximately 150 nm) and a hollow mesoporous structure, which was confirmed by elemental mapping showing the existence of C, O, N, K, and Fe (Fig. 1C). Subsequently, TPP was chemically crosslinked with PEI, and its highly cationic properties were leveraged to modify the HPB nanozymes to achieve mitochondrial targeting following cellular uptake. ^{1}H NMR indicated that the peak with a chemical shift of d represented the C-H bond adjacent to the carbonyl group, the peak of b is attributed to the C-H bond adjacent to the amide bond, and the O-H peak of TPP on the carboxyl group at position 12.33 disappeared (Fig. 1D–S1), confirming a successful chemical reaction between TPP and PEI. The FTIR spectra revealed the disappearance of the characteristic TPP peak at 1715 cm^{-1} and the attenuation of the PEI amine peak at 3275 cm^{-1}. Combined with the emergence of a new characteristic peak at 1637 cm^{-1} (corresponding to the C=O stretching vibration) (Fig. 1E), this demonstrates that TPP and PEI achieved covalent conjugation by forming amide bonds via carboxylic acid-amine condensation reactions. PEI-TPP was then assembled with the HPB nanozymes (HPBPT) via ultrasonic electrostatic bonding. Finally, the CM NPs and HPBPT nanozymes were physically extruded after sonication to obtain CM@HPBPT nanozymes. Surface zeta potential data (Fig. 1F) demonstrated the successful binding of PEI-TPP to HPB nanozymes (negative-to-positive charge shift) and subsequent chondrocyte membrane coating (positive-to-negative charge shift). DLS (Fig. 1G) confirmed minimal size change upon CM coating (HPB: 183.5 nm, HPBPT: 193.5 nm, CM: 189.6 nm, CM@HPBPT: 202.9 nm), TEM identified the core-shell structure of CM@HPBPT (Fig. 1H), further indicating that CM were successfully coated on the outer layer of HPBPT. Finally, the ultraviolet absorption spectra depict the characteristic peak of HPB at approximately 740 nm for both HPBPT and CM@HPBPT (Fig. 1I), providing further evidence of successful CM NP coating. These findings demonstrate the successful synthesis of the CM@HPBPT nanozymes.

3.2. Cell selection, immune escape, and mitochondrial targeting of CM@HPBPT nanozymes

HPB nanozymes were labeled with FITC for visualization to further verify the targeted delivery of CM@HPBPT nanozymes to chondrocyte mitochondria. Mouse macrophages and chondrocytes were cultured with either HPBPT or CM@HPBPT nanozymes to determine the effect of the chondrocyte membrane coating on cell selection. Fluorescence intensity analysis showed that the fluorescence intensity of CM@HPBPT chondrocytes was significantly higher than that of HPBPT, and that of HPBPT in RAW264.7 cells was significantly higher than that of CM@HPBPT (Fig. 2A and B). Flow cytometry also showed that the uptake of CM@HPBPT by chondrocytes was significantly higher than that of RAW 264.7 (Fig. S3A). The internalization rate of HPBPT in RAW 264.7 was higher than that in chondrocytes, which was primarily related to the strong non-specific phagocytosis ability of macrophages and the strong interaction between unmodified nanoparticles and immune cells [43,44]. In contrast, the chondrocytes themselves do not possess non-specific phagocytic ability, therefore internalization is significantly reduced without the camouflage of chondrocyte membranes. The higher internalization of CM@HPBPT in chondrocytes than that of HPBPT highlights the role of chondrocyte membranes in targeting chondrocytes. The cell membrane is crucial for cell recognition and facilitates substance exchange through membrane fusion [45]. Leveraging this property, emerging membrane biomimetic technology has endowed nanoparticles with multifaceted capabilities, such as immune evasion and targeted recognition [46]. Different cell membrane sources distinctly influence cellular uptake efficiency, targeting precision, and biological interactions. For instance, erythrocyte membrane camouflage leverages immune evasion properties to prolong nanoparticle circulation time, while tumor cell membrane coating exploits homotypic targeting to enhance nanoparticle binding to homologous cancer cells and improve uptake efficiency [47]. In this study, compared with coated with other membranes (mouse nucleus pulposus membrane and macrophage membrane), we used chondrocyte membrane camouflage to modify HPBPT, so that they had chondrocyte specific targeting ability, and cellular uptake of HPBPT was significantly higher (Fig. S3B and S3C). This strategy improves uptake of chondrocytes and enhances intracellular delivery of HPBPT. We labeled CM NPs with DiO and chondrocytes with DiI to validate the potential mechanism of CM@HPBPT nanozyme delivery, we labeled CM NPs with DiO and chondrocytes with DiI. The results confirmed the fusion of CM NPs with homologous chondrocytes (Fig. 2C). This suggests that CM@HPBPT nanozymes deliver HPBPT nanozymes into the cytoplasm through membrane fusion and internalization. These findings are consistent with those of an existing study [48].

Furthermore, flow cytometry analysis indicated that the complement of endocytosis inhibitors failed to affect the cellular uptake of the CM@HPBPT nanozymes, whereas low temperatures significantly inhibited it (Fig. 2D and E). These findings suggest membrane fusion to be the primary mechanism of cellular uptake. Previous studies have suggested that lysosomal degradation and phagocytosis hinder the efficacy of most metal nanozymes within cells [49]. We hypothesized that the membrane fusion pathway enables the CM@HPBPT nanozymes to evade lysosomes, thereby enhancing their therapeutic potential. To investigate lysosomal escape, we performed co-localization analysis of lysosomes with HPBPT or CM@HPBPT. We observed minimal co-localization of CM@HPBPT with lysosomes (Fig. 2F, upper panel, G), whereas most of the internalized HPBPT co-localized with lysosomes (Fig. 2F, lower panel, G). These findings indicate that the CM@HPBPT nanozymes can avoid lysosomal degradation through lysosomal escape. Finally, we performed a co-localization analysis of mitochondria with CM@HPB and CM@HPBPT to verify the mitochondrial-targeting ability. Fluorescence microscopy images revealed significantly higher co-localization between CM@HPBPT and mitochondria than between CM@HPB and mitochondria (Fig. 2H and I). This demonstrates the superior mitochondrial-targeting ability of the CM@HPBPT nanozymes.

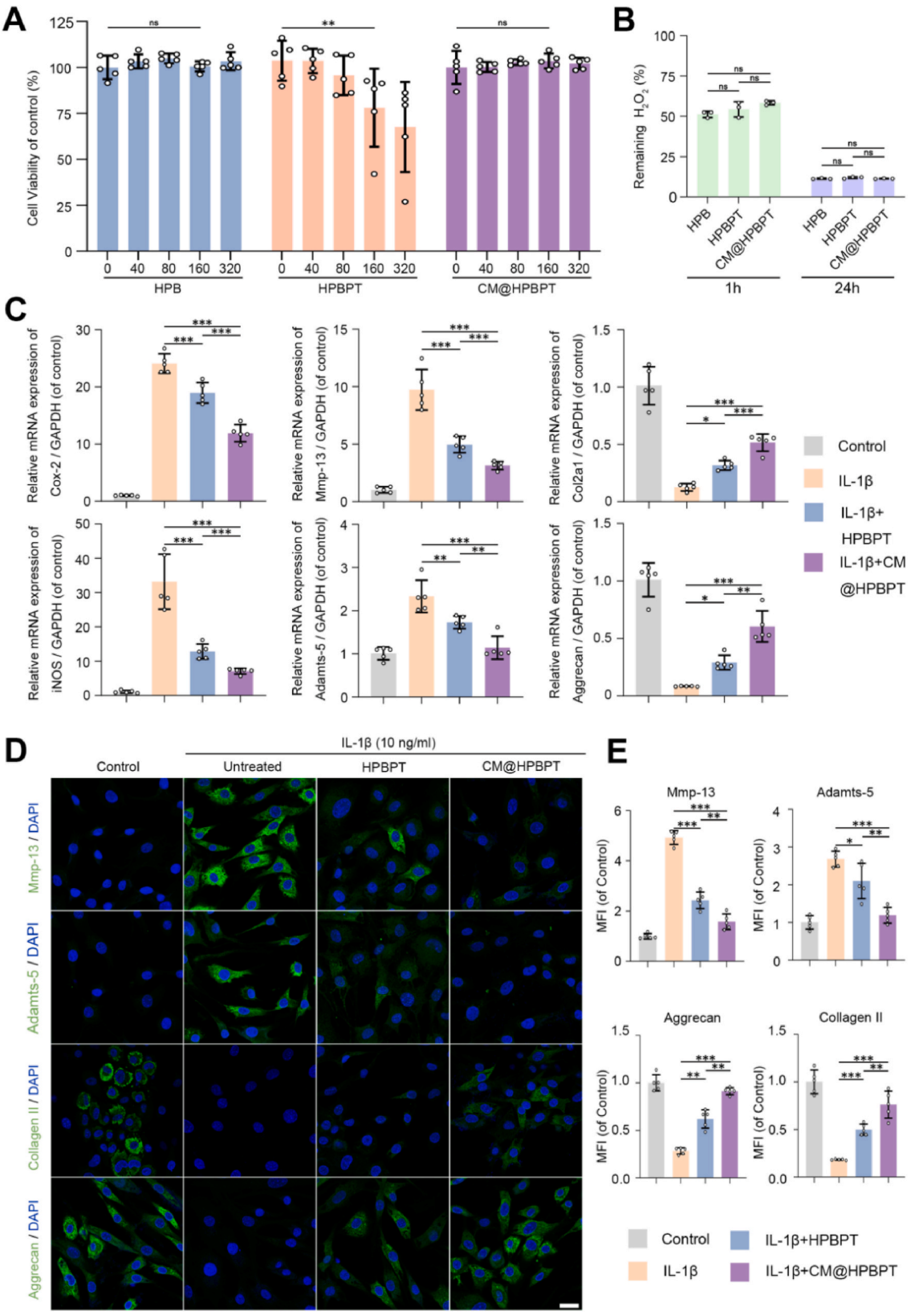

Fig. 3. CM@HPBPT nanozymes improved damaged chondrocyte function. (A) Cytotoxicity of HPB, HPBPT, and CM@HPBPT against chondrocytes after 24 h incubation at the indicated concentrations (n = 5). (B) H_2O_2 scavenging behavior of HPB, HPBPT, and CM@HPBPT after 1 and 24 h incubation at 80 μg/mL (n = 3). (C) RT-qPCR with detection of Cox-2, iNOS, Aggrecan, Col2a1, Mmp-13, and Adamts-5 expression in chondrocytes incubated with each group (n = 5). The expression was normalized to the control. (D–E) Immunofluorescence (IF) staining and quantification indicating Adamts-5, Mmp-13, collagen II, and aggrecan levels in chondrocytes (scale bar, 25 μm; n = 5). ***p < 0.001; **p < 0.01; *p < 0.05, ns, p > 0.05.

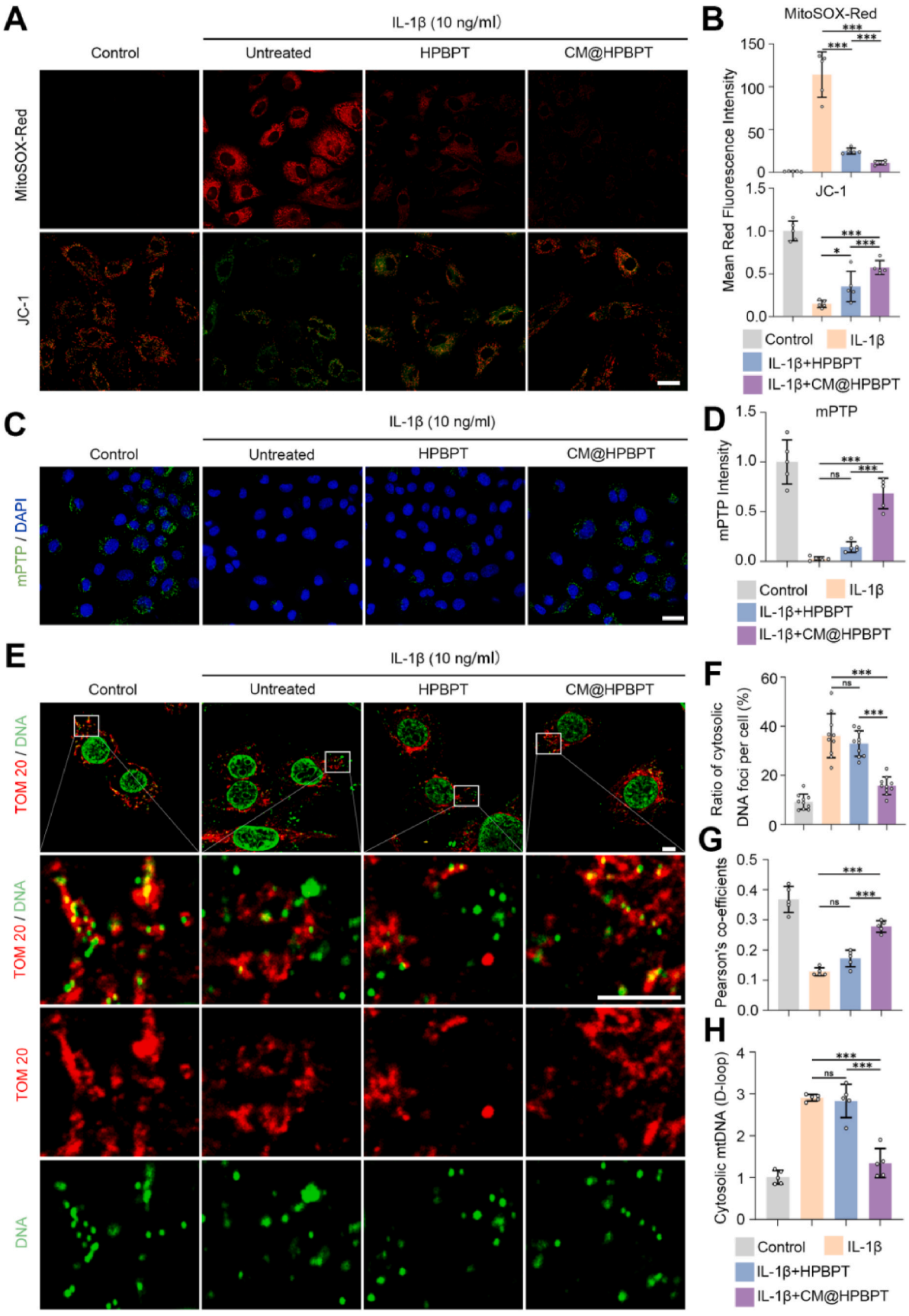

(caption on next page)

Fig. 4. CM@HPBPT nanozymes reduced mtDNA leakage in damaged chondrocytes. (A–B) Chondrocytes from each group were stained with MitoSOX-Red and JC-1. (JC-1, red and green; MitoSOX-Red, red; scale bar, 25 μm; n = 5). (C–D) mPTP assay kit was used to detect mPTP opening in chondrocytes. The lower the fluorescence of calcein, the higher the degree of mPTP opening (Fluorescence intensity of calcein, green; nuclei, blue. Scale bar, 25 μm; n = 5). (E) Representative confocal microscopy images of mitochondria (TOM 20) and mtDNA; when mtDNA is non-colocalized with mitochondria, it means that mtDNA has leaked into the cytoplasm (TOM 20, red; DNA, green. Scale bar, 5 μm). (F) Ratio of the cytosolic DNA foci per cell (n = 10). (G) Pearson's coefficients of the mitochondria and mtDNA (excluding the nucleus, n = 5). (H) RT-qPCR of the levels of cytosolic mtDNA (D-loop region) present in the cytosolic fraction of chondrocytes, normalized to the average of the control (n = 5). ***$p < 0.001$; *$p < 0.05$; ns, $p > 0.05$. (For interpretation of the references to colour in this figure legend, the reader is referred to the Web version of this article.)

These findings collectively demonstrate that CM@HPBPT nanozymes can effectively target chondrocytes and deliver HPBPT to their mitochondria via a membrane fusion mechanism.

3.3. CM@HPBPT nanozymes improving damaged chondrocytes

We evaluated the effects of the CM@HPBPT nanozymes on inflammatory degenerative chondrocytes. First, cytotoxicity assays revealed that HPBPT exhibited increased cytotoxicity at 80 μg/mL compared to HPB, but this cytotoxicity decreased upon CM coating (CM@HPBPT) (Fig. 3A). Through above findings, 80 μg/mL was chosen as the therapeutic dose for the subsequent experiments. HPB nanozymes exhibit a potent ROS scavenging efficiency [50]. Considering the potential impact of HPB-nanozyme modification on ROS scavenging ability, we assessed the hydrogen peroxide removal efficiency of HPB, HPBPT, and CM@HPBPT at 1 and 24 h. The scavenging efficiency was higher in all groups at 24 h, and the CM coating had no significant effect on the scavenging efficiency (Fig. 3B), suggesting that CM@HPBPT retained good ROS scavenging activity. To assess its therapeutic effects, we employed interleukin-1β (IL-1β)-induced inflammatory degenerative chondrocytes as a model [51]. RT-qPCR analysis revealed that CM@HPBPT treatment greatly reduced the expression of inflammation-related genes (*iNOS* and *Cox-2*) and ECM degradation-related genes (*Adamts-5* and *Mmp-13*) and enhanced ECM synthesis-related gene expression (aggrecan and collagen II) compared to HPBPT alone (Fig. 3C). Confocal fluorescence microscopy further confirmed these findings, demonstrating that CM@HPBPT significantly reduced ECM-degradation-related protein expression and increased ECM-synthesis related protein expression compared with HPBPT (Fig. 3D and E). In conclusion, our data strongly suggest that CM@HPBPT nanozymes effectively ameliorate chondrocyte damage.

3.4. CM@HPBPT nanozymes reduce mtROS in damaged chondrocytes, preventing mtDNA leakage and cGAS-STING-NF-κB activation

Based on previous research linking OA to mitochondrial dysfunction in chondrocytes [39], we evaluated the effects of IL-1β on mitochondrial function. MitoSOX staining revealed significant mtROS accumulation in IL-1β-induced chondrocytes (indicated by higher red fluorescence intensity). As a key indicator of mitochondrial function, the mitochondrial membrane potential was also significantly eliminated (indicated by the lower red fluorescence intensity of JC-1 staining) in these chondrocytes. Notably, CM@HPBPT nanozymes greatly reduced mtROS and restored the mitochondrial membrane potential compared to HPBPT nanozymes (Fig. 4A and B).

This enhanced therapeutic effect of the CM@HPBPT nanozymes likely stems from the precise targeting of mtROS in chondrocytes. A previous study showed that mitochondrial dysfunction can induce the opening of mPTP, which disrupts the membrane potential and triggers inflammatory and apoptotic pathways [52]. The mPTP opening was assessed using the mPTP calcein fluorescence kit, where decreased fluorescence indicated increased opening. Consistent with mitochondrial dysfunction, IL-1β significantly weakened calcein fluorescence in chondrocytes, suggesting increased mPTP opening (Fig. 4C and D). Notably, the CM@HPBPT nanozymes effectively reversed mPTP opening, whereas HPBPT did not. mPTP opening is a key factor that results in mtDNA leakage from the mitochondria to the cytoplasm, further fueling inflammation [53]. Hence, we evaluated the alterations in mtDNA. Colocalization staining of mtDNA and mitochondria illustrated a significant enhancement in cytosolic mtDNA and a reduction in colocalization in IL-1β-induced chondrocytes (Fig. 4E, F, G), indicating increased mtDNA leakage. Importantly, the CM@HPBPT nanozymes significantly reversed mtDNA leakage, whereas HPBPT did not. The D-loop is closely related to mtDNA replication and is often used to measure mtDNA levels [54]. Therefore, we verified the levels of mtDNA leakage by assessing the D-loop content in the cytoplasm (Fig. 4H). This suggests that the CM@HPBPT nanozymes improve mitochondrial mPTP function and prevent mtDNA leakage. In summary, our study demonstrated that CM@HPBPT nanozymes can improve mitochondrial function by scavenging mtROS in chondrocytes, which reversed mPTP opening and reduced mtDNA leakage.

Notably, compared with HPBPT alone, CM@HPBPT nanozymes substantially reduced the fluorescence intensity exerted by STING and decreased cGAS and p-STING protein levels, suggesting potent inhibition of the cGAS-STING pathway (Fig. 5 A, B, E). We observed that the positive number of P65 and levels of both p-P65 and p-IκBα proteins were highly expressed following IL-1β stimulation (Fig. 5C, D, F), indicating the activation of the NF-κB pathway.

In summary, under IL-1β stimulation, chondrocyte mitochondria exhibit excessive accumulation of mtROS and altered mitochondrial membrane potential, which leads to a significant increase in mPTP opening. This enables the leakage of mtDNA from the mitochondrial interior into the cytoplasm, where cytosolic mtDNA is recognized by cGAS, activating the STING and NF-κB signaling pathways. The activation of NF-κB disrupts the balance of cartilage ECM-related proteins (ADAMTS-5, MMP-13, Collagen II, Aggrecan) and aggravates OA progression (Fig. 5G). Notably, the CM@HPBPT nanozyme targeting chondrocyte mitochondria precisely scavenges mtROS, restores mitochondrial membrane potential, reduces mPTP opening, significantly decreases mtDNA leakage, inhibits the cGAS-STING-NF-κB signaling pathway, and reestablishes cartilage ECM homeostasis. Collectively, therapeutic intervention with CM@HPBPT nanozyme dynamically regulates mtROS levels, restores mitochondrial membrane potential, modulates mPTP opening and mtDNA leakage, and ultimately attenuates inflammatory responses by influencing the cGAS-STING-NF-κB signaling pathway.

3.5. Preparation, characterization, and therapeutic effects of the hybrid hydrogel

Hydrogels have been used to improve the short half-lives and strong toxicities of metal nanozymes [55]. GA self-assembles into hydrogels (GA hydrogels) with desirable ROS-scavenging properties [56]; however, its poor mechanical strength hinders its clinical application. GelMA offers superior strength with drug delivery and tissue regeneration capabilities [57]. In this study, we used GelMA to enhance the strength of GA hydrogels (GGM hydrogels) and loaded them with CM@HPBPT to obtain chondrocyte membrane biomimetic nanozyme-incorporated GGM hydrogels (GGM@CM@HPBPT hydrogels). Fig. 6A shows the gelatinization properties of each hydrogel group. The FTIR spectra indicated that the GGM inside had a strong hydrogen bonding interaction, confirming the stable chemical structure of GGM (Fig. 6B). SEM revealed a porous but relatively loose microstructure of GA, whereas GGM and GGM@CM@HPBPT displayed

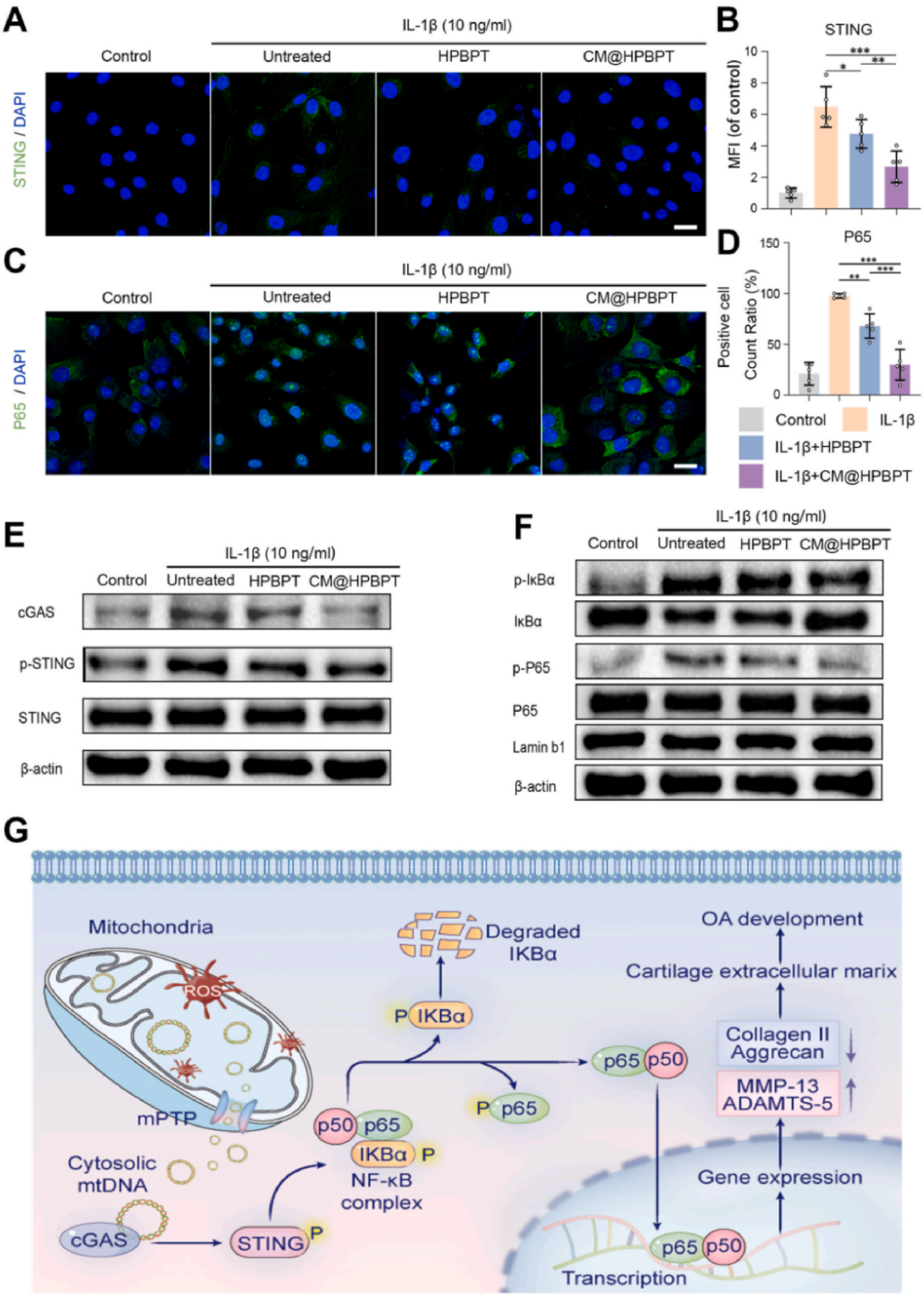

Fig. 5. CM@HPBPT nanozymes alleviate the activation of cGAS-STING-NF-κB signaling caused by mtDNA leakage in damaged chondrocytes. (A–B) IF staining and quantification indicating STING levels in chondrocytes (n = 5). (C–D) IF staining and quantification indicating P65 levels in chondrocytes (n = 5). (E–F) Representative western blot images of p-STING, STING, cGAS, IκBα, p-IκBα, p-P65, and P65 expression in chondrocytes. (G) Mechanism illustration: The activation of the mtDNA-cGAS-STING-NF-κB signaling pathway induced by mtROS. ***p < 0.001; **p < 0.01; *p < 0.05. Scale bar, 25 μm.

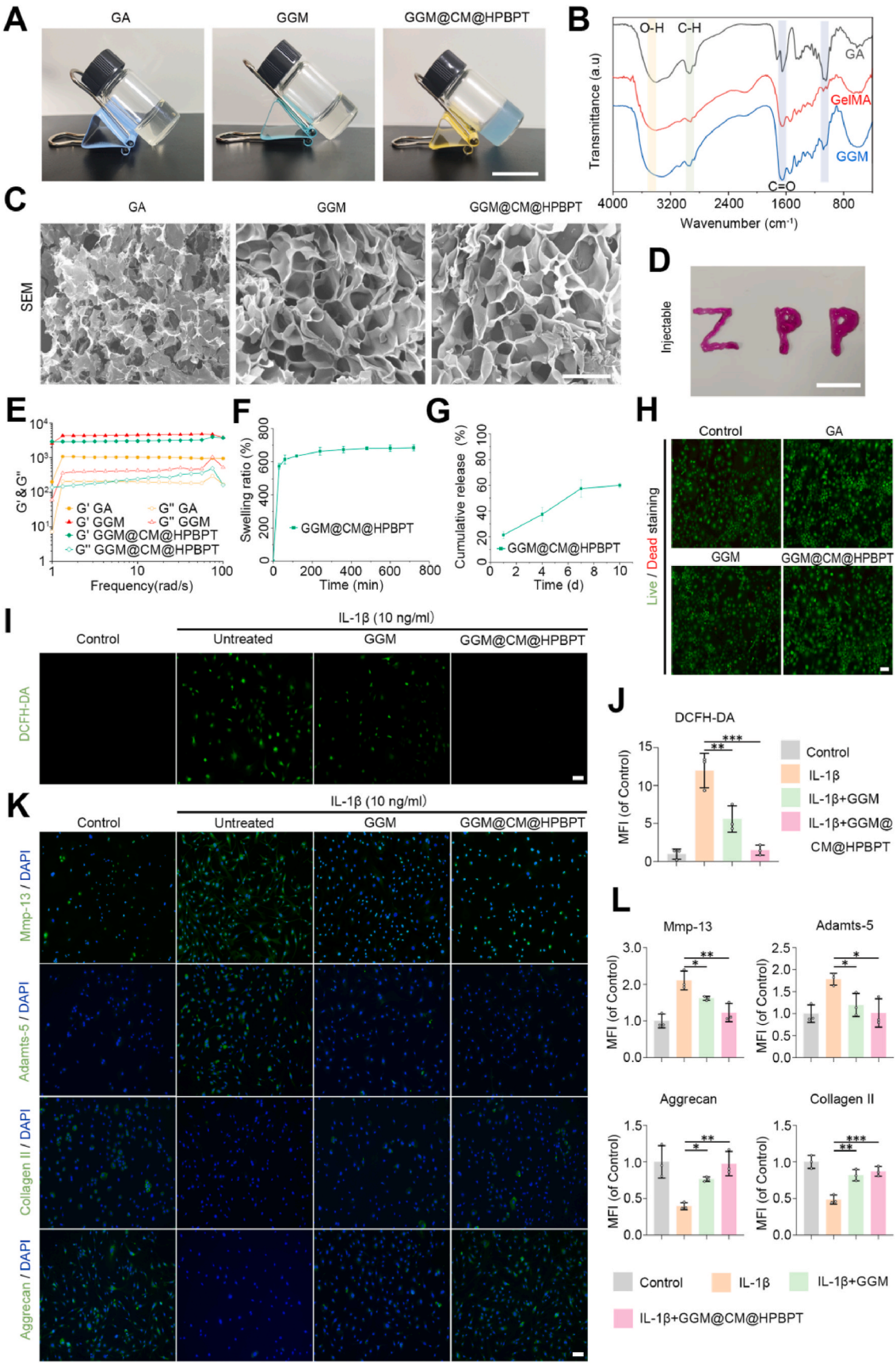

(caption on next page)

Fig. 6. Preparation, characterization, and in-vitro experiment of GGM@CM@HPBPT hydrogel. (A) Macroscopic photographs of GA, GGM, and GGM@CM@HPBPT hydrogels (scale bar, 1 cm). (B) FTIR spectra for GA, GelMA, and GGM hydrogels. (C) SEM images of GA, GGM, and GGM@CM@HPBPT hydrogels (scale bar, 100 μm). (D) injectability test of GGM hydrogel (GGM hydrogel artificially stained by rhodamine B; scale bar, 1 cm). (E) Frequency scan tests (from 1 to 100 Hz) of the different hydrogels. (F) Swelling ratio of GGM@CM@HPBPT (n = 3). (G) Cumulative release of CM@HPBPT from the GGM@CM@HPBPT hydrogel in PBS at 37 °C (n = 3). (H) Live/dead staining of chondrocytes cultured on the surface of GA, GGM, and GGM@CM@HPBPT hydrogels for 24 h (scale bar, 100 μm). (I–J) Representative microscopic images of chondrocytes stained with DCFH-DA indicating the ROS levels in chondrocytes (DCFH-DA, green; scale bar, 100 μm). Statistical analysis of MFI of DCFH-DA in each group is shown (n = 3). (K–L) IF staining and quantification indicating Mmp-13, collagen II, Adamts-5, and aggrecan levels in chondrocytes (scale bar, 100 μm; n = 3). ***p < 0.001; **p < 0.01; *p < 0.05. (For interpretation of the references to colour in this figure legend, the reader is referred to the Web version of this article.)

uniform and interconnected porous structures (Fig. 6C), suggesting a strengthening effect of GelMA on GA. GGM hydrogels exhibited good injectability without needle blockage (Fig. 6D). Mechanical property analysis demonstrated that the storage modulus (G′) of all hydrogels exceeded the loss modulus (G″) in the frequency range of 1–100.

rad/s, suggesting their elastic behavior. Notably, the GGM@CM@HPBPT hydrogel exhibited significantly higher strength than the GA hydrogel (Fig. 6E). The swelling test showed that the GGM@CM@HPBPT hydrogel maintained its structure after 6 h (Fig. 6F). In the release test, the release rate of the GGM@CM@HPBPT hydrogel gradually decreased, and the release efficiency was approximately 60 % after 7 days (Fig. 6G). Subsequently, we evaluated the effects of hydrogels on chondrocytes. Live/dead staining confirmed the minimal cytotoxicity of all the hydrogels (Fig. 6H). DCFH-DA staining revealed that GGM@CM@HPBPT reduced IL-1β-induced ROS levels in chondrocytes compared to GGM alone (Fig. 6I and J). Finally, we assessed the therapeutic effect of GGM@CM@HPBPT hydrogels on IL-1β-induced damaged chondrocytes using confocal fluorescence microscopy. GGM@CM@HPBPT hydrogels significantly reduced ADAMTS-5 and MMP-13 expressions and increased aggrecan and collagen II expressions compared with GGM alone (Fig. 6K and L). In conclusion, the GGM@CM@HPBPT hydrogel demonstrated a more pronounced therapeutic effect, which can be attributed to the loaded CM@HPBPT nanozymes.

3.6. Effect and mechanism of action of the GGM@CM@HPBPT hydrogel on OA

To continue examining the in-vivo performance of the GGM@CM@HPBPT hydrogel in treating OA, we established OA mice model via ACLT surgery [36]. We investigated whether GGM, CM@HPBPT, and GGM@CM@HPBPT hydrogels could inhibit OA progression in these mice (Fig. 7A). HE staining revealed no discernible changes in the spleen, heart, lung, liver, and kidney in all treatment groups compared to the sham group, suggesting the in-vivo safety of all treatment conditions (Figs. S3 and S4). The pathological changes in each group were assessed by HE and SO staining at 4 and 8 weeks, with further confirmation using the OARSI score (0–6) [42]. Compared with the ACLT untreated group, all treatment groups exhibited reduced cartilage destruction, lower OARSI scores, and less severe OA changes. Notably, the GGM@CM@HPBPT hydrogel demonstrated significantly more pronounced effects than GGM alone (Fig. 7B, C, E).

Micro-CT analysis was conducted to evaluate the progression of OA by examining the tibial subchondral bone [41]. At 8 weeks, the CM@HPBPT and GGM@CM@HPBPT treatment groups displayed reduced morphological alterations and osteophyte formation (Fig. 7D). Quantification revealed that treatment with GGM@CM@HPBPT and CM@HPBPT significantly reduced the trabecular bone pattern factor and increased the bone volume fraction, indicating an improved bone structure. The effect of GGM was insignificant (Fig. 7F and G), which was likely owing to the CM@HPBPT nanozymes that precisely scavenged mtROS in chondrocytes.

We performed IF staining on related proteins to systematically validate the therapeutic effects and molecular mechanisms of GGM@CM@HPBPT hydrogel in delaying OA progression. Aggrecan and Collagen II, as core components of the cartilage ECM, are crucial for maintaining cartilage structure and function, serving as key biomarkers for evaluating OA progression [58]. Compared with the ACLT group, the GGM@CM@HPBPT group exhibited significantly elevated expression levels of Aggrecan and Collagen II (Fig. 8A–C), indicating substantial improvement in cartilage ECM levels in OA mice. INOS, a critical inflammatory mediator, activates inflammatory signaling pathways, such as NF-κB and induces ECM imbalance in chondrocytes, making it an essential indicator in assessing inflammatory expression in OA [59]. The GGM@CM@HPBPT group showed markedly reduced iNOS expression levels compared to the ACLT group (Fig. 8A–D), suggesting significant alleviation of cartilage inflammation in OA mice.8-OHdg is a product of ROS attack on DNA, which causes oxidative stress. ROS levels can be assessed using 8-OHdg [60]. The GGM@CM@HPBPT group demonstrated significantly lower 8-OHdg levels than the ACLT group (Fig. 8A–E), indicating substantial mitigation of ROS-mediated oxidative stress in OA mice. STING, a core molecule of the cGAS-STING pathway, drives OA-related inflammation, cartilage degradation, and abnormal bone remodeling by sensing DNA damage signals, serving as a key marker for assessing cGAS-STING pathway activation [61]. P65, the primary transcriptional activation subunit of the NF-κB complex, plays a pivotal role in OA progression by regulating inflammation, matrix degradation, and apoptosis, and is a central biomarker for evaluating NF-κB pathway activity [62]. Compared with the ACLT group, the GGM@CM@HPBPT group exhibited significantly reduced STING and P65 levels (Fig. 8A–F, G), suggesting inhibition of the cGAS-STING-NF-κB signaling pathway in OA mice. In conclusion, our in-vivo experiments further demonstrate that GGM@CM@HPBPT can attenuate ROS-induced oxidative damage in OA chondrocytes, thereby suppressing the cGAS-STING-NF-κB signaling pathway, improving cartilage ECM homeostasis, and delaying OA progression.

4. Conclusion

We constructed a dual-targeted composite nanozyme, CM@HPBPT, and then incorporated nanozymes to form GGM@CM@HPBPT, which achieved a curative effect on OA by precisely scavenging mtROS and protecting cartilage. While the hybrid hydrogel exerted ROS scavenging activity in the joint cavity, the slow-released CM@HPBPT targeted the mitochondria in chondrocytes and efficiently scavenged mtROS. Reduced levels of mtROS in the damaged chondrocytes reversed the opening of mPTP and decreased mtDNA leakage to the cytoplasm, which inhibited the cGAS-STING-NF-κB pathway, which in turn hindered inflammatory storms in the damaged chondrocytes (Fig. 9). The experiments confirmed that CM@HPBPT nanozymes achieved precise scavenging of mtROS in chondrocytes to inhibit mtDNA-cGAS-STING-NF-κB signaling, and the GGM@CM@HPBPT hydrogel exhibited an excellent curative effect and ultimately alleviated osteoarthritis in mice model. In conclusion, we used a combination of dual-targeting nanozymes and a multifunctional hydrogel to address the limitations of conventional nanozymes. Achieving precise scavenging of mtROS to treat OA sheds light on the fundamental processes underlying mitochondrial impairment and inflammatory responses in OA and introduces an innovative nanotherapeutic approach for treating mitochondria-related disorders.

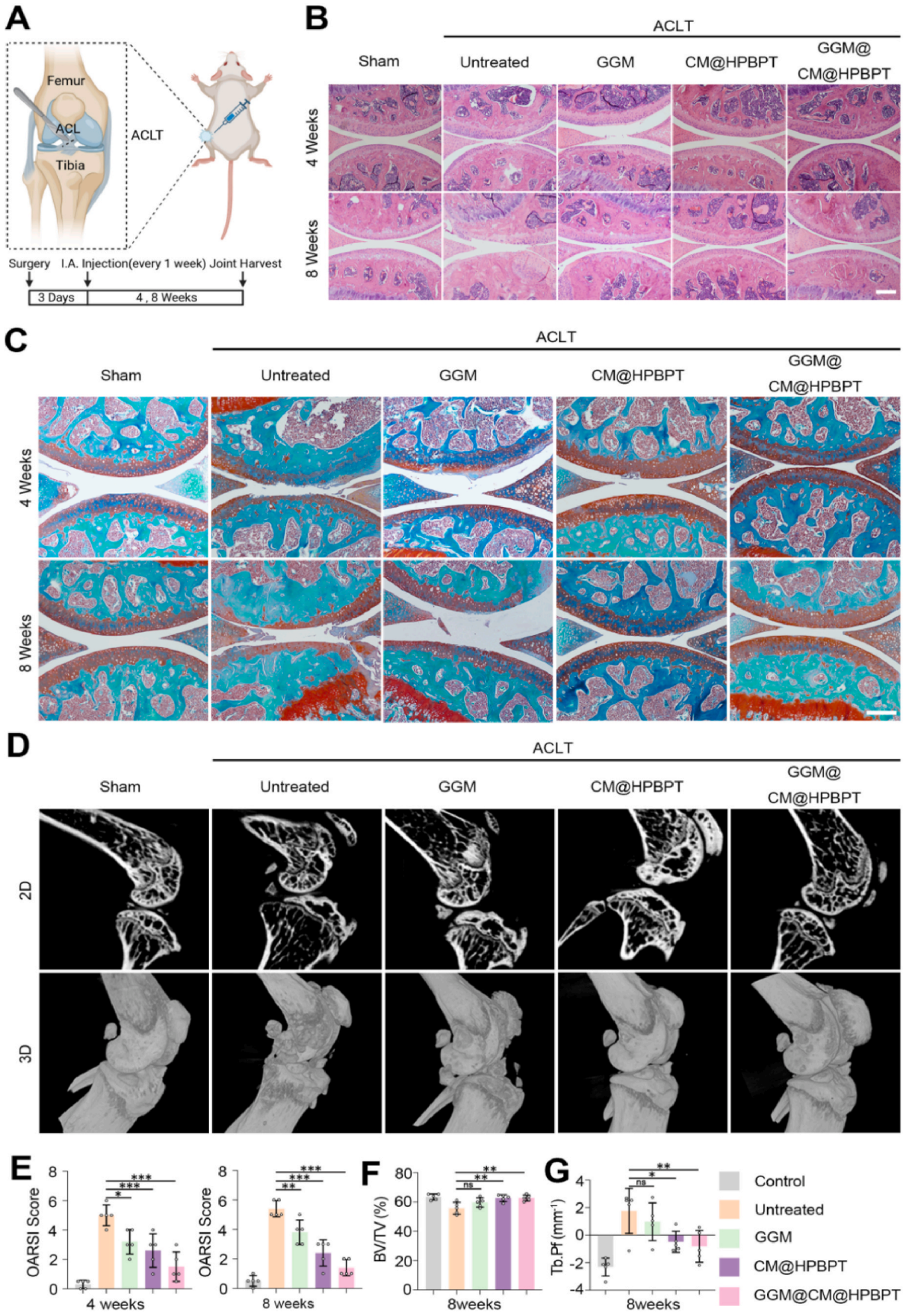

Fig. 7. Morphological changes caused by GGM@CM@HPBPT hydrogel treatment on OA in mice. (A) Schematic illustration of ACLT mice subjected to different treatments. (B) HE staining of the knee joints at 4 or 8 weeks. (C) SO staining of the knee joints at 4 and 8 weeks. (D) Micro-CT images of 2D and 3D of knee joints in each group at 8 weeks. (E) OARSI joint scores at 4 and 8 weeks (n = 5). (F–G) Quantitative analysis of BV/TV (F) and Tb.Pf (G) in mice (n = 5). ***$p < 0.001$; **$p < 0.01$; *$p < 0.05$, ns, $p > 0.05$. Scale bar, 50 μm.

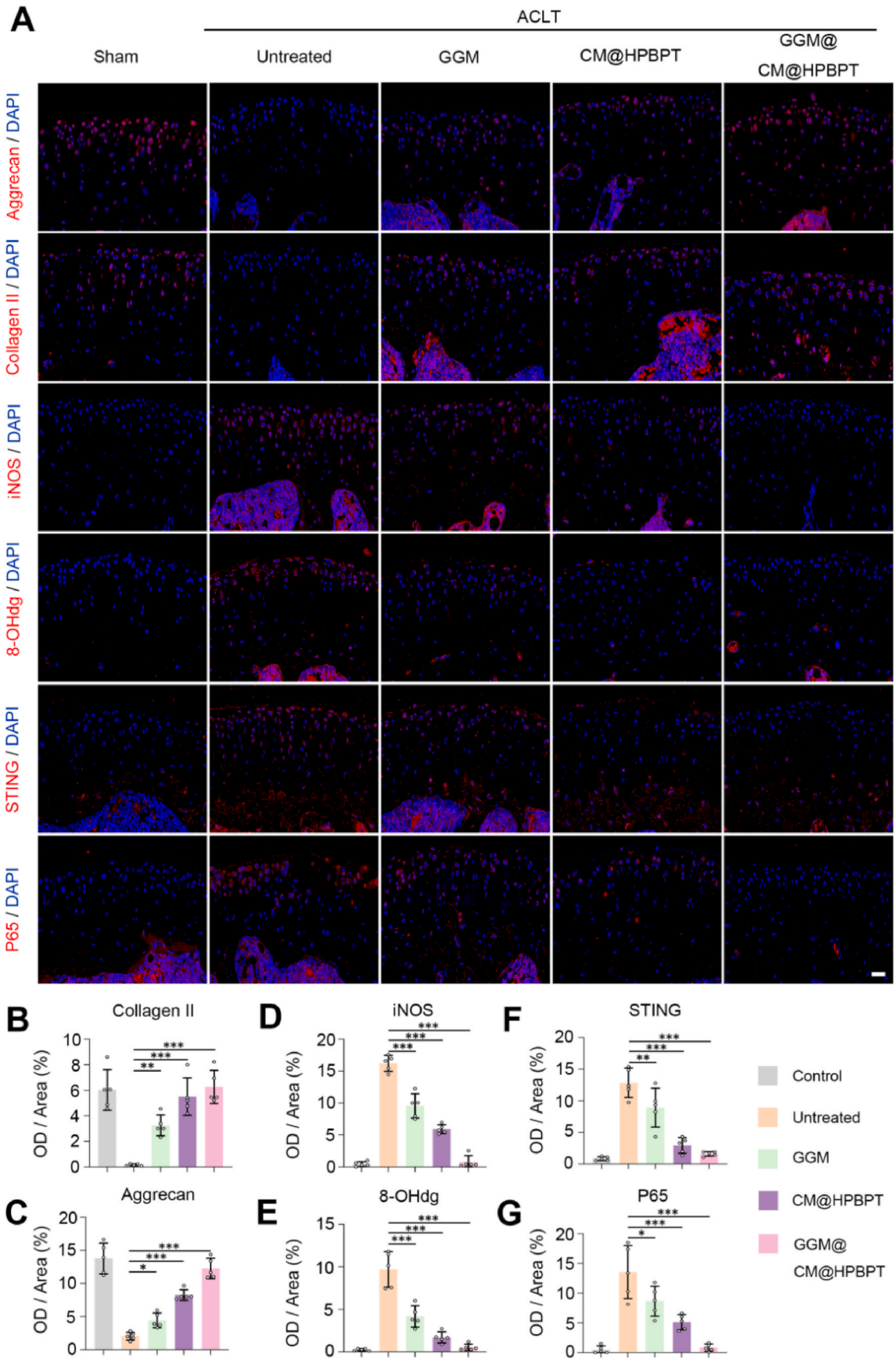

Fig. 8. Pathophysiological changes and potential mechanisms of action of the GGM@CM@HPBPT hydrogel on OA in mice. (A) IF staining of aggrecan, collagen II, iNOS, 8-OHdg, STING, and P65 levels in the indicated treated knee joints (n = 5). (B–G) Quantification (OD/area) of collagen II, aggrecan, iNOS, 8-OHdg, STING, and P65 levels in the indicated treated knee joints (n = 5). ***p < 0.001; **p < 0.01; *p < 0.05. Scale bar, 50 μm.

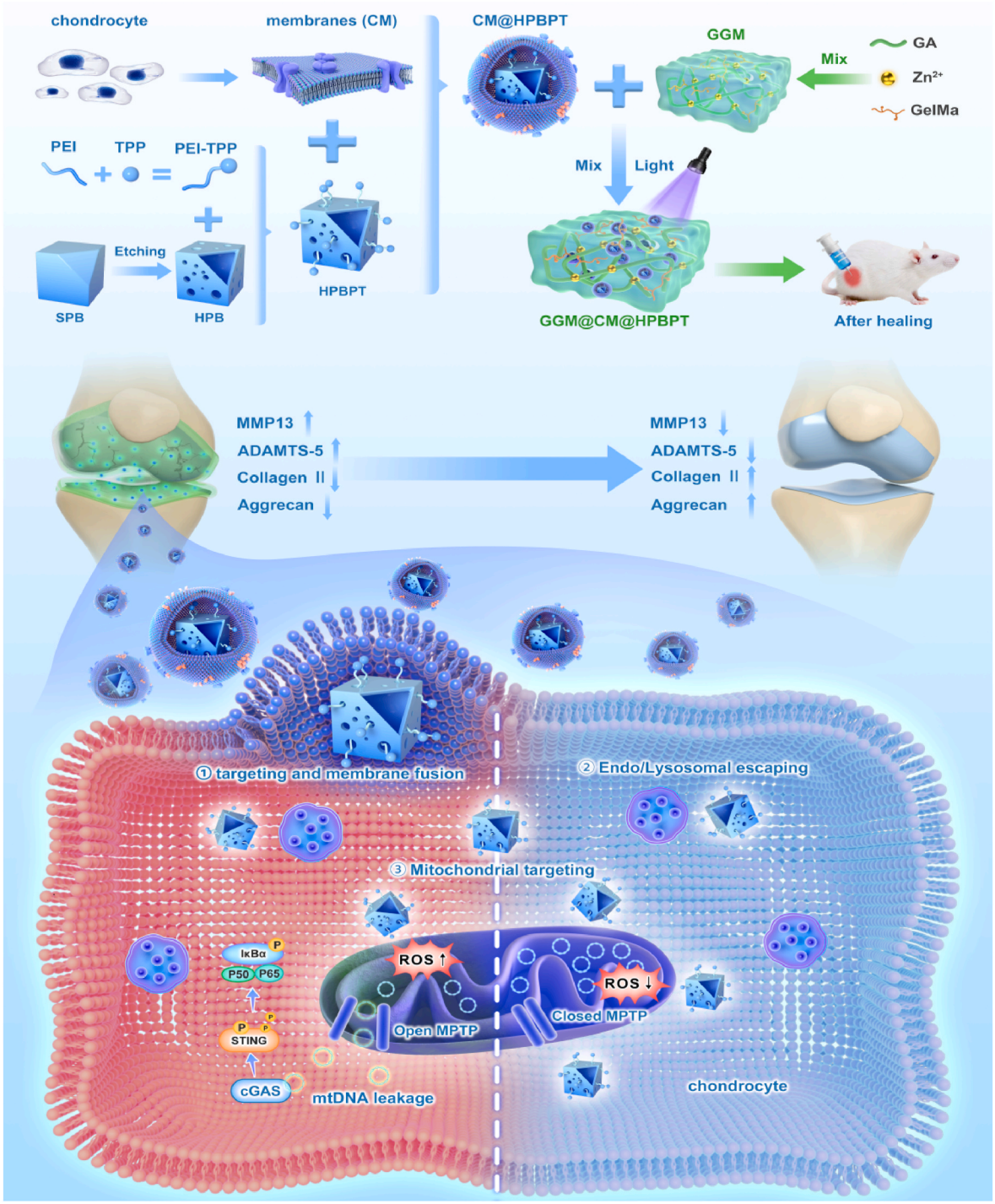

Fig. 9. Schematic illustration of GGM@CM@HPBPT: Precise targeting of mitochondrial ROS in chondrocytes to delay OA progression. (A) Preparation of GGM@CM@HPBPT hydrogel. (B) GGM@CM@HPBPT hydrogel with the slow release of CM@HPBPT and its therapeutic mechanism in OA.

CRediT authorship contribution statement

Yong Fan: Writing – review & editing, Writing – original draft, Data curation, Conceptualization. **Zexuan Niu:** Methodology, Formal analysis, Data curation. **Li Yin:** Resources, Investigation, Formal analysis. **Longtao Yao:** Validation, Software. **Sheyuan Ding:** Investigation. **Yu Tong:** Visualization, Validation, Supervision. **Jiao Wang:** Software. **Zheping Hong:** Supervision. **Jihang Chen:** Funding acquisition. **Qiong Zhang:** Visualization, Project administration, Funding acquisition. **Lichen Ji:** Software, Methodology. **Jiaxin Chen:** Validation, Supervision, Project administration, Conceptualization. **Chen Xia:** Writing – review & editing, Project administration, Funding acquisition, Conceptualization. **Qing Bi:** Writing – review & editing, Project administration, Funding acquisition, Conceptualization.

Data availability

All data generated or analyzed during this study are included in this published article and its supplementary information files.

Declaration of competing interest

The authors declare that they have no known competing financial interests or personal relationships that could have appeared to influence the work reported in this paper.

Acknowledgements

The study was sponsored by National Natural Science Fund of China (82302679), Zhejiang Province Major Science and Technology Project (2021C03078), Zhejiang Provincial Natural Science Foundation of China (LQ23H060008, TGY24H060025), Zhejiang Province Public Technology Application Research Project (LGF22H060029), National Science and Technology Resource Sharing Service Platform Project of China (YCZYPT202303), Zhejiang Province Medical and Health Science and Technology Project (2022KY500), and Zhejiang Province Traditional Chinese Medicine Science and Technology Project (2024035416, 2022ZB034).

Appendix A. Supplementary data

Supplementary data to this article can be found online at https://doi.org/10.1016/j.mtbio.2025.101778.

Data availability

Data will be made available on request.

References

[1] J.N. Katz, K.R. Arant, R.F. Loeser, Diagnosis and treatment of hip and knee osteoarthritis, JAMA 325 (6) (2021).
[2] D.J. Hunter, S. Bierma-Zeinstra, Osteoarthritis, Lancet 393 (10182) (2019) 1745–1759.
[3] Q. Yao, et al., Osteoarthritis: pathogenic signaling pathways and therapeutic targets, Signal Transduct. Targeted Ther. 8 (1) (2023).
[4] J.G.B. Primrose, et al., REST, RCOR1 and RCOR2 expression is reduced in osteoarthritic chondrocytes and contributes to increasing MMP13 and ADAMTS5 expression through upregulating HES1, Cell. Signal. 109 (2023).
[5] A. Fan, et al., Inhibition of fibroblast activation protein ameliorates cartilage matrix degradation and osteoarthritis progression, Bone Research 11 (1) (2023).
[6] I.A. Jones, et al., Intra-articular treatment options for knee osteoarthritis, Nat. Rev. Rheumatol. 15 (2) (2018) 77–90.
[7] M. Giacomello, et al., The cell biology of mitochondrial membrane dynamics, Nat. Rev. Mol. Cell Biol. 21 (4) (2020) 204–224.
[8] A. Tocchi, et al., Mitochondrial dysfunction in cardiac aging, Biochim. Biophys. Acta Bioenerg. 1847 (11) (2015) 1424–1433.
[9] M. Arra, et al., LDHA-mediated ROS generation in chondrocytes is a potential therapeutic target for osteoarthritis, Nat. Commun. 11 (1) (2020).
[10] P.R. Coryell, B.O. Diekman, R.F. Loeser, Mechanisms and therapeutic implications of cellular senescence in osteoarthritis, Nat. Rev. Rheumatol. 17 (1) (2020) 47–57.
[11] Q. Zhang, et al., Nano-brake halts mitochondrial dysfunction cascade to alleviate neuropathology and rescue alzheimer's cognitive deficits, Adv. Sci. 10 (7) (2023).
[12] F.J. Blanco, A.M. Valdes, I. Rego-Pérez, Mitochondrial DNA variation and the pathogenesis of osteoarthritis phenotypes, Nat. Rev. Rheumatol. 14 (6) (2018) 327–340.
[13] L.D. Aarreberg, et al., Interleukin-1β induces mtDNA release to activate innate immune signaling via cGAS-STING, Mol. Cell 74 (4) (2019) 801–815, e6.
[14] T. Yang, et al., Nitisinone attenuates cartilage degeneration and subchondral osteoclastogenesis in osteoarthritis and concomitantly inhibits the cGAS/STING/NF-κB pathway, Eur. J. Pharmacol. 965 (2024).
[15] Y. Zhao, et al., DNA damage and repair in age-related inflammation, Nat. Rev. Immunol. 23 (2) (2022) 75–89.
[16] Y. Yang, H. Zhang, Intra-articular injection of nanomaterials for the treatment of osteoarthritis: from lubrication function restoration to cell and gene therapy, Adv. Funct. Mater. 34 (30) (2024).
[17] Shaoshuai Song, Jingyi Zhang, Ya Fang, Wenxing Li, Hong Zeng, Zhen Fang, Tianchang Wang, Youzhuan Xie, Chaozong Liu, Jinwu Wang, Nerve–bone crosstalk manipulates bone organoid development and bone regeneration: a review and perspectives, Organoid Research 1 (1) (2025) 8294.
[18] X. Wang, Q. Li, H. Yang, Effect of radiation sterilisation on the structure and antibacterial properties of antimicrobial peptides, Biomater Transl 4 (1) (2023 Mar 28) 51–61.
[19] J. Li, et al., Targeted and responsive biomaterials in osteoarthritis, Theranostics 13 (3) (2023) 931–954.
[20] Y. Huang, J. Ren, X. Qu, Nanozymes: classification, catalytic mechanisms, activity regulation, and applications, Chem. Rev. 119 (6) (2019) 4357–4412.
[21] W. Zhang, et al., Prussian blue nanoparticles as multienzyme mimetics and reactive oxygen species scavengers, J. Am. Chem. Soc. 138 (18) (2016) 5860–5865.
[22] W. Hou, et al., Excavating bioactivities of nanozyme to remodel microenvironment for protecting chondrocytes and delaying osteoarthritis, Bioact. Mater. 6 (8) (2021) 2439–2451.
[23] B. Rathore, et al., Nanomaterial designing strategies related to cell lysosome and their biomedical applications: a review, Biomaterials 211 (2019) 25–47.
[24] P. Chen, et al., A plant-derived natural photosynthetic system for improving cell anabolism, Nature 612 (7940) (2022) 546–554.
[25] Q. Li, Y. Huang, Mitochondrial targeted strategies and their application for cancer and other diseases treatment, Journal of Pharmaceutical Investigation 50 (3) (2020) 271–293.
[26] L. Fan, et al., Exosome-based mitochondrial delivery of circRNA mSCAR alleviates sepsis by orchestrating macrophage activation, Adv. Sci. 10 (14) (2023).
[27] Q. Truong Hoang, et al., Piezocatalytic 2D WS2 nanosheets for ultrasound-triggered and mitochondria-targeted piezodynamic cancer therapy synergized with energy metabolism-targeted chemotherapy, Adv. Mater. 35 (18) (2023).
[28] C. Gao, F. Lyu, Y. Yin, Encapsulated metal nanoparticles for catalysis, Chem. Rev. 121 (2) (2020) 834–881.
[29] M. Wang, et al., Articular cartilage repair biomaterials: strategies and applications, Materials Today Bio 24 (2024).
[30] Z. Zhou, et al., Silk fibroin-based biomaterials for cartilage/osteochondral repair, Theranostics 12 (11) (2022) 5103–5124.
[31] R. Li, S. Qiu, W. Yang, Z. Rao, J. Chen, Y. Yang, Q. Zhu, X. Liu, Y. Bai, D. Quan, A comparative study of human and porcine-derived decellularised nerve matrices, Biomater Transl 4 (3) (2023 Sep 28) 180–195.
[32] C. Shen, et al., Silk fibroin-based hydrogels for cartilage organoids in osteoarthritis treatment, Theranostics 15 (2) (2025) 560–584.
[33] Jing Zhao, Fuming Shen, Shihao Sheng, Jian Wang, Miaomiao Wang, Fuxiao Wang, Yingying Jiang, Yingying Jing, Ke Xu, Jiacan Su, Cartilage-on-chip for osteoarthritis drug screening, Organoid Research 1 (1) (2025) 8461.
[34] L. Pang, et al., Treatment with mesenchymal stem cell-derived nanovesicle-containing gelatin methacryloyl hydrogels alleviates osteoarthritis by modulating chondrogenesis and macrophage polarization, Adv. Healthcare Mater. 12 (17) (2023).
[35] X. Li, et al., Research progress in hydrogels for cartilage organoids, Adv. Healthcare Mater. 13 (22) (2024).
[36] C. Fang, et al., Diterbutyl phthalate attenuates osteoarthritis in ACLT mice via suppressing ERK/c-fos/NFATc1 pathway, and subsequently inhibiting subchondral osteoclast fusion, Acta Pharmacol. Sin. 43 (5) (2021) 1299–1310.
[37] D. Nie, et al., Cancer-cell-membrane-coated nanoparticles with a yolk–shell structure augment cancer chemotherapy, Nano Lett. 20 (2) (2019) 936–946.
[38] M. Zhu, et al., Active-oxygenating hollow Prussian blue nanosystems loaded with biomacromolecules for photodynamic/photothermal therapy of cancer and alleviating hypoxic tumors, Mater. Des. (2024) 237.
[39] L. Zhang, et al., Reprogramming mitochondrial metabolism in synovial macrophages of early osteoarthritis by a camouflaged meta-defensome, Adv. Mater. 34 (30) (2022).
[40] V. Zecchini, et al., Fumarate induces vesicular release of mtDNA to drive innate immunity, Nature 615 (7952) (2023) 499–506.
[41] J. Liu, et al., Exosomal transfer of osteoclast-derived miRNAs to chondrocytes contributes to osteoarthritis progression, Nature Aging 1 (4) (2021) 368–384.
[42] S.S. Glasson, et al., The OARSI histopathology initiative – recommendations for histological assessments of osteoarthritis in the mouse, Osteoarthr. Cartil. 18 (2010) S17–S23.
[43] A. Aderem, D.M. Underhill, Mechanisms of phagocytosis in macrophages, Annu. Rev. Immunol. 17 (1999) 593–623.
[44] S. Chen, et al., Macrophages in immunoregulation and therapeutics, Signal Transduct. Targeted Ther. 8 (1) (2023).
[45] B.P. Dyett, et al., Fusion dynamics of cubosome nanocarriers with model cell membranes, Nat. Commun. 10 (1) (2019).
[46] L. Chen, et al., Recent progress in targeted delivery vectors based on biomimetic nanoparticles, Signal Transduct. Targeted Ther. 6 (1) (2021).
[47] H. uo, M. Guo, Z. Xia, Z. Shao, Membrane-coated nanoparticles as a biomimetic targeted delivery system for tumour therapy, Biomater Transl 5 (1) (2024 Mar 28) 33–45.
[48] R. Deng, R. Z, Z. Zhang, Y. Chen, M. Yang, Y. Lin, J. Ye, N. Li, H. Qin, X. Yan, J. Shi, F. Yuan, S. Song, Z. Xu, Y. Song, J. Fu, B. Xu, G. Nie, J.K. Yu, Chondrocyte membrane–coated nanoparticles promote drug retention and halt cartilage damage in rat and canine osteoarthritis, Sci. Transl. Med. 16 (2024) 735.
[49] E. Blanco, H. Shen, M. Ferrari, Principles of nanoparticle design for overcoming biological barriers to drug delivery, Nat. Biotechnol. 33 (9) (2015) 941–951.
[50] Z. Xu, et al., Thermosensitive hydrogel incorporating prussian blue nanoparticles promotes diabetic wound healing via ROS scavenging and mitochondrial function restoration, ACS Appl. Mater. Interfaces 14 (12) (2022) 14059–14071.
[51] K. Feng, et al., Cartilage progenitor cells derived extracellular vesicles-based cell-free strategy for osteoarthritis treatment by efficient inflammation inhibition and extracellular matrix homeostasis restoration, J. Nanobiotechnol. 22 (1) (2024).
[52] D.B. Zorov, M. Juhaszova, S.J. Sollott, Mitochondrial reactive oxygen species (ROS) and ROS-induced ROS release, Physiol. Rev. 94 (3) (2014) 909–950.
[53] M. Bonora, C. Giorgi, P. Pinton, Molecular mechanisms and consequences of mitochondrial permeability transition, Nat. Rev. Mol. Cell Biol. 23 (4) (2021) 266–285.
[54] H. Liu, et al., Prohibitin 1 regulates mtDNA release and downstream inflammatory responses, EMBO J. 41 (24) (2022).

[55] P. Lu, et al., Harnessing the potential of hydrogels for advanced therapeutic applications: current achievements and future directions, Signal Transduct. Targeted Ther. 9 (1) (2024).
[56] Y. Qian, et al., Immunoregulation in diabetic wound repair with a photoenhanced glycyrrhizic acid hydrogel Scaffold, Adv. Mater. 34 (29) (2022).
[57] Y. Piao, et al., Biomedical applications of gelatin methacryloyl hydrogels, Engineered Regeneration 2 (2021) 47–56.
[58] Moliner A. Pueyo, K. Ito, F. Zaucke, D.J. Kelly, M. de Ruijter, J. Malda, Restoring articular cartilage: insights from structure, composition and development, Nat. Rev. Rheumatol 21 (2025 Mar 28) 291–308.
[59] W.H. Robinson, et al., Low-grade inflammation as a key mediator of the pathogenesis of osteoarthritis, Nat. Rev. Rheumatol. 12 (10) (2016) 580–592.
[60] Z.-R. Yang, et al., Endogenous stimuli-responsive separating microneedles to inhibit hypertrophic scar through remodeling the pathological microenvironment, Nat. Commun. 15 (1) (2024).
[61] Q. Guo, et al., STING promotes senescence, apoptosis, and extracellular matrix degradation in osteoarthritis via the NF-κB signaling pathway, Cell Death Dis. 12 (1) (2021).
[62] J. Han, et al., Moderate mechanical stress suppresses chondrocyte ferroptosis in osteoarthritis by regulating NF-κB p65/GPX4 signaling pathway, Sci. Rep. 14 (1) (2024).